Article

# Chiral dual-annihilator model for controllable photon upconversion and multi-dimensional optical modulation

Honghan Ji[1,2], Zhiwang Luo[1], Xuefeng Yang [1], Xue Jin [1], Tonghan Zhao [1] & Pengfei Duan [1,2]

Triplet-triplet annihilation photon upconversion seeks efficient conversion of low-energy photons to high-energy emission. However, the triplet-triplet annihilation photon upconversion system faces limitations in emission gamut because efficient triplet-triplet energy transfer between sensitizer and annihilator relies on triplet energy matching, making it challenging to realize multi-channel luminescence and multi-dimensional optical control. Here, to overcome this barrier, we propose a chiral dual-annihilator model, which mitigates the restriction of energy matching and achieves facile manipulation of circularly polarized luminescence through a dual-channel triplet-triplet energy transfer process. A theoretical equation for quantifying the overall triplet-triplet energy transfer efficiency and the energy flow between the sensitizer and two kinds of annihilators is proposed. Its accuracy is demonstrated by fine-controlling the emission bandwidth of triplet-triplet annihilation photon upconversion (average error less than 4.5%) in the experimental aspect. In addition, by introducing chiral liquid crystals, the dual-annihilator model achieves data coding and multi-dimensional optical encryption applications. This dual-annihilator model deepens the understanding of energy flow and lays the foundation for accurate, multidimensional modulation of photon upconversion.

Triplet-triplet annihilation photon upconversion (TTA-UC) integrates photon energy combination and exciton coupling through a complex triplet transfer and annihilation process[1-4]. Accordingly, low-energy excitation sources can produce high-energy emission light, thus avoiding the issues of the photobleaching effect and spontaneous fluorescence interference in traditional high-energy excitation systems[5-7]. With its advantages, TTA-UC has profound significance in the fundamental research of optical materials[8-10]. The Dexter energy transfer in the TTA-UC system relies on electron exchange[11,12], where the overlap of the electron wave function and triplet states determines the efficiency[13,14]. Effective energy transmission requires strict symmetry of triplets,

reducing the flexibility of the system's expansion, especially for multi-color light output[15-18]. Although the emission colors of annihilators can be adjusted through organic synthesis, a complex synthesis process is often unavoidable. Additionally, the optical properties of the resulting annihilators tend to be unpredictable. Further development demands breaking through the deep physical bottleneck caused by energy symmetry in this system[19-21]. Previous studies studied a thermal-activated triplet-triplet energy transfer (TA-TTET) approach to circumvent energy mismatch[22]. However, precisely controlling the energy flow dynamics to achieve tunable multicolor luminescence remains a significant challenge within current TTA-UC frameworks.

[1]CAS Key Laboratory of Nanosystem and Hierarchical Fabrication, National Center for Nanoscience and Technology (NCNST), No.11, ZhongGuanCun BeiYi-Tiao, Beijing, People's Republic of China. [2]University of Chinese Academy of Sciences, No. 1 Yanqihu East Road, Huairou District, Beijing, People's Republic of China. e-mail: zhaoth@nanoctr.cn; duanpf@nanoctr.cn

Apart from the luminescence color, multi-dimensional modulation on photonic states plays a significant role in information encoding[23–25]. The wavelength-dominant single-dimension encoding severely restricts the potential of TTA-UC for advanced applications requiring high information density. To address this, researchers have focused on introducing circular polarization property as an orthogonal information dimension[26–29]. For instance, upconverted circularly polarized luminescence (UCCPL) based on upconversion nanoparticles (UCNPs) in chiral liquid crystals (CLCs) has been reported. The dissymmetry factor[30], i.e., $g_{lum} = 2 \times (I_L - I_D)/(I_L + I_D)$ denoting the intensities difference between left-handed ($I_L$) and right-handed ($I_D$) circularly polarized light, reached ~0.5, achieving encrypted photonic barcode[31]. Nevertheless, the luminescence efficiency and wavelength tenability of UCNPs are still a challenge.

In this work, we establish a dual-annihilator model in toluene solution and CLCs, realizing tunable energy flow and luminescence gamut regulation through dual-path energy transfer (Fig. 1). This approach is expected to extend the traditional TTA-UC systems by decoupling energy transfer from the constraints of energy level symmetry[32,33], providing a more flexible and efficient pathway for photon conversion[34]. Typically, a dual-path energy transfer system is constructed by combining the triplet energy-mismatched annihilator (DPA) and the triplet energy-matched annihilator/sensitizer pair (BDP/PtTPBP). Although the triplet energy level of DPA is higher than that of PtTPBP, DPA can participate in the triplet dynamic processes through TA-TTET[22,35]. A set of kinetic equations regarding the energy flow in the dual-annihilator model is derived. The experimental results demonstrate that the color of UCPL, from blue to yellow can be accurately controlled based on these equations with errors less than 5.0%. In addition, we design a series of TTA-UC micromatrices within CLCs[36–40], producing effective UCCPL with $g_{lum}$ value at -1.0. And a notable discrepancy was observed between UCCPL and downshifting circularly polarized luminescence (DSCPL). This divergence can be ascribed to the inherent differences in their luminescence mechanisms, as well as the unique synergistic effects resulting from dual-path energy transfer processes. Compared to the traditional TTA-UC system, the dual-annihilator model not only retains the polarization characteristic of TTA-UCCPL for information hiding but also leverages excitation-related emission color differentiation to prevent data tampering. On the basis of this feature, anti-counterfeiting patterns, graphical encoding, and flexible TTA-UCCPL films with high-level and multi-dimensional input and output light are fabricated. This chiral dual-annihilator model opens new avenues for advanced data storage encryption and efficient processing methods.

## Results

### Dynamic derivation of the dual-annihilator model

The dual-annihilator model is constructed by combining PtTPBP with an energy-mismatched annihilator (DPA) and an energy-matched annihilator (BDP), where the DPA/PtTPBP system is considered to realize the TTA-UC process by crossing the energy barrier of 0.16 eV through TA-TTET[35]. The dynamic process of the dual-annihilator model was thoroughly analyzed and discussed in Supplementary Notes 1 and 2. The disparity in two annihilators excited triplet populations and singlet annihilation processes are predominantly influenced by the rate at which they gain triplet energy of sensitizer ($k_{ET}T_D$). Hence, the exploration of the dual-annihilator model mainly focuses on the energy transfer process from the sensitizer to these two annihilators in Supplementary Equation 2 (Supplementary Note 1)[21]. The proposed relationship is subsequently employed to assess the efficiency of TTET ($\Phi_{TTET}$) using the following Eq. 1,

$$\Phi_{TTET} = \frac{k_{ET1} \times C_{(DPA)} + k_{ET2} \times C_{(BDP)}}{k_D^T + k_{ET1} \times C_{(DPA)} + k_{ET2} \times C_{(BDP)}}$$
$$= 1 - \frac{1}{1 + k_{ET1} \times \tau_0 \times C_{(DPA)} + k_{ET2} \times \tau_0 \times C_{(BDP)}} \quad (1)$$

Where $k_D^T$ and $\tau_0$ represent the spontaneous decay rate and triplet lifetime of the sensitizer in the absence of the annihilators, $k_{ET1}$ and $k_{ET2}$ are the TTET rates of DPA and BDP, respectively, and $C_{(DPA)}$ and $C_{(BDP)}$ are the concentrations of DPA and BDP, respectively. This model describes the triplet energy flow relationship, which allows for predicting the synergistic effect of dual annihilators and modulating the TTA-UC emission color.
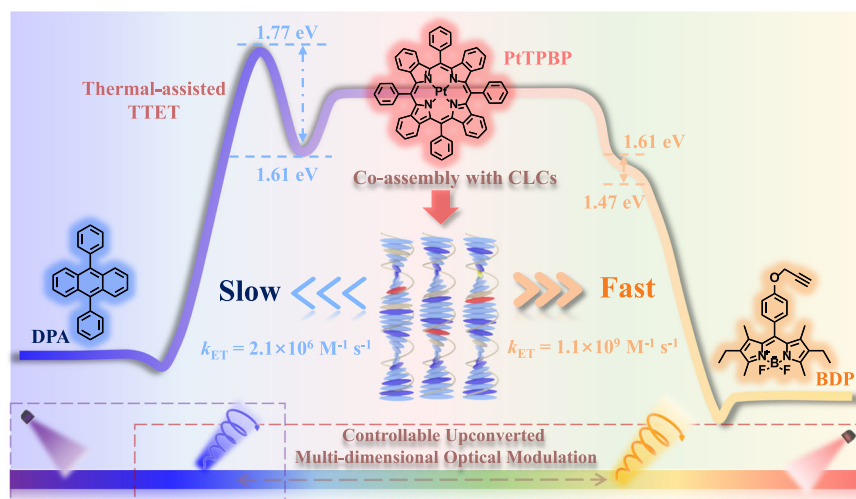


**Fig. 1 | Chiral dual-annihilator model for controllable photon upconversion and multi-dimensional optical modulation.** The energy level and energy transfer roadmap of the sensitizer and annihilator in the dual-annihilator model. The energy-mismatched annihilator (DPA) implements the triplet-triplet annihilation photon upconversion (TTA-UC) process by means of thermally-activated triplet-triplet energy transfer (TA-TTET). The dual-annihilator model was introduced into the chiral nematic liquid crystals (CLCs) microenvironment. The triple-state energy competition between DPA and BDP realizes the coordinated adjustment of the color of upconverted circularly polarized luminescence (UCCPL). The color of UCCPL and downshifting circularly polarized luminescence (DSCPL) can be clearly distinguished upon excitation of 639 and 365 nm light, respectively.
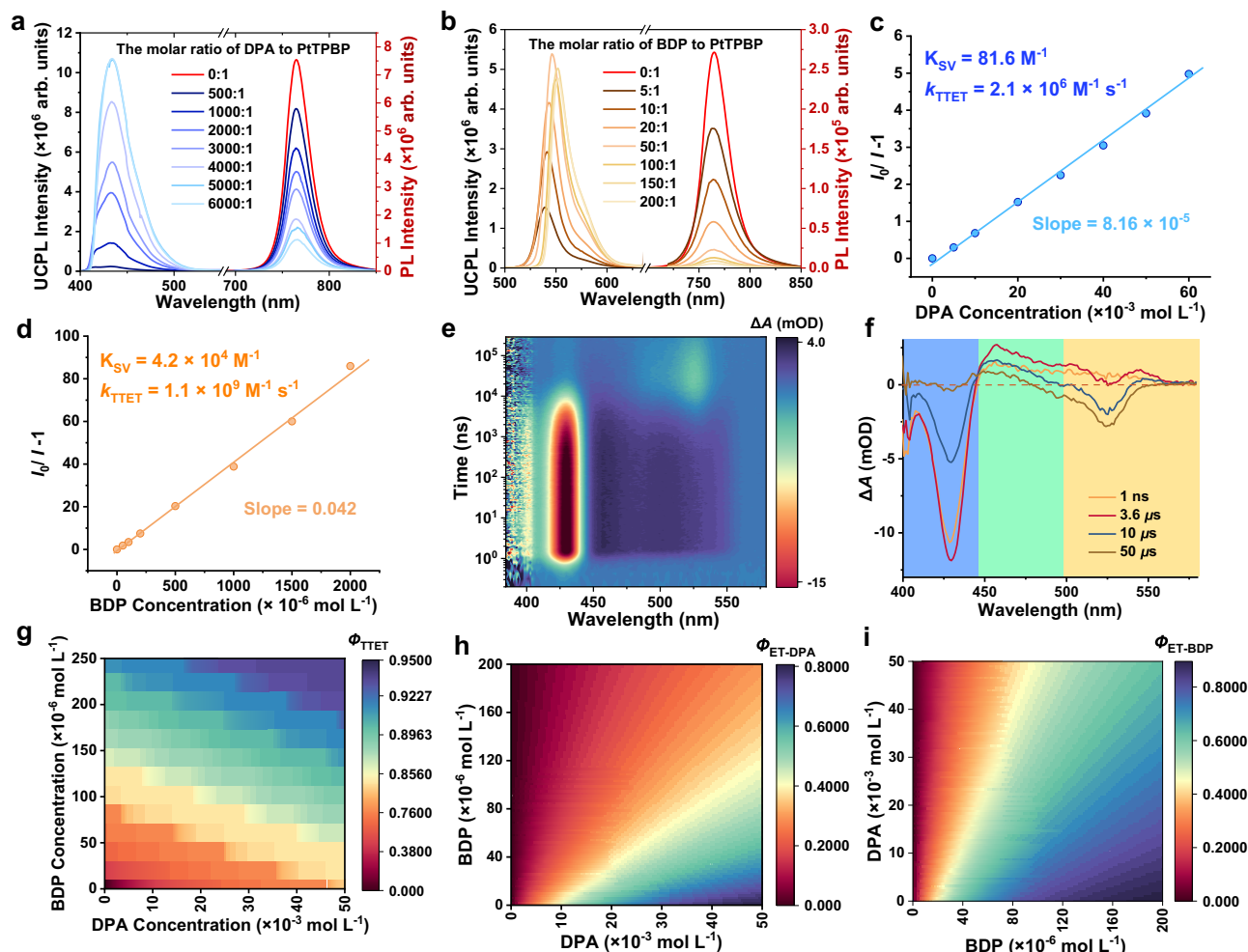
**Fig. 2 | Kinetic analyses of the TTA-UC process of DPA/PtTPBP, BDP/PtTPBP, and DPA/BDP/PtTPBP system in deaerated toluene. And the derivation process of energy flow of the dual-annihilator model.** Upconverted photoluminescence (UCPL) spectra of **a** DPA/PtTPBP and **b** BDP/PtTPBP with different molar ratios under excitation of 639 nm laser with the power density of 1.6 and 0.9 W cm$^{-2}$, respectively. [PtTPBP] = 1.0 × 10$^{-5}$ mol L$^{-1}$. Signals around 774 nm are the emission of the sensitizer. The Stern-Volmer plot of **c** DPA/PtTPBP and **d** BDP/

PtTPBP. **e** 2D and **f** 1D transient absorption spectra of dual-annihilator model in deaerated toluene. The power density of the 635 nm laser was 475 mW cm$^{-2}$. [PtTPBP] = 1.0 × 10$^{-5}$ mol L$^{-1}$, [DPA] = 5.0 × 10$^{-3}$ mol L$^{-1}$, [BDP] = 2.5 × 10$^{-4}$ mol L$^{-1}$. **g** Calculated energy transfer efficiencies ($\Phi_{TTET}$) of dual annihilators with different concentrations. The simulation is deduced through the coupled rate equation of the system's dynamic process. [PtTPBP] = 1.0 × 10$^{-5}$ mol L$^{-1}$, [DPA] = 0 − 5.0 × 10$^{-2}$ mol L$^{-1}$, [BDP] = 0−2.5 × 10$^{-4}$ mol L$^{-1}$. Calculated $\Phi_{TTET}$ of **h** DPA and **i** BDP.

To validate the proposed TTET process, we prepared samples in deaerated toluene and performed the following experiments. When [PtTPBP] = 1.0 × 10$^{-5}$ mol L$^{-1}$, the UCPL spectra of DPA/PtTPBP (molar ratio 5000:1) and BDP/PtTPBP (molar ratio 50:1) systems were studied. The emission peaks were observed at 440 and 544 nm, respectively. The UCPL intensities as a function of excitation power density exhibited a slope transition from ~2 to ~1, indicating excitation thresholds are approximately 1.3 and 0.6 W cm$^{-2}$ for DPA/PtTPB and BDP/PtTPBP, respectively (Supplementary Fig. 1). We further examined the effects of varying DPA and BDP concentrations on UCPL intensity and the phosphorescence decay of the sensitizer (Fig. 2a, b and Supplementary Fig. 2), revealing distinct quenching behaviors (the Stern-Volmer constants (K$_{SV}$) and the triplet energy transfer rate ($k_{TTET}$) between DPA and BDP[5,11]. Although high concentration of DPA causes slight suppression on fluorescence intensity, the UPCL of DPA/PtTPBP shows significant enhancement because of the improved $\Phi_{TTET}$ and $\Phi_{TTA}$ (Fig. 2a, Supplementary Figs. 3a, b and 4, Supplementary Table 3). In addition, the evolution of UCPL intensities of DPA/PtTPBP with the concentrations of DPA at 5.0 × 10$^{-3}$ and 6.0 × 10$^{-2}$ mol L$^{-1}$ present good photostability under continuous irradiation of 639 nm laser (Supplementary Fig. 5). By resolving Supplementary Equations 5 and 6, the

DPA/PtTPBP system possesses quenching parameters with K$_{SV}$ of 81.6 M$^{-1}$ and $k_{TTET}$ of 2.1 × 10$^6$ M$^{-1}$ s$^{-1}$ (Fig. 2c), while BDP/PtTPBP exhibited stronger quenching performance with K$_{SV}$ of 4.2 × 10$^4$ M$^{-1}$ and $k_{TTET}$ of 1.1 × 10$^9$ M$^{-1}$ s$^{-1}$ (Fig. 2d). The low $k_{TTET}$ demands a large number of DPA existing Furthermore, we utilized transient absorption (TA) spectroscopy to dig into the triplet flow behavior. As shown in Supplementary Figs. 5a and 6a, ground-state bleaches (GSB) originating from the singlet transition of PtTPBP can be observed at 430 nm. Subsequently, PtTPBP exhibits excited-state absorption (ESA) of T$_1$-T$_n$ at 460 nm with the intensity of 5 mOD. With the addition of DPA, DPA/PtTPBP system still shows the ESA signal ~460 nm but the intensity slightly decreases, probably due to the TTET from PtTPBP to DPA (Supplementary Figs. 6b and 7b). Similarly, BDP/PtTPBP exhibits weak intensity at 460 nm, confirming the TTET process between PtTPBP and annihilators. Moreover, a strong stimulated emission (SE) signal originating from the UCPL of BDP can be detected at 525 nm which is undetectable in DPA/PtTPBP system (Supplementary Figs. 6c and 7c), agreeing with the previous demonstrations of lower quenching ability of DPA. To investigate the triplet dynamics, we carried out the time-resolved phosphorescence decay measurements of PtTPBP with/without annihilators. With the presence of DPA, the decay kinetics

possess a fast component. Additionally, the decay time of this fast component gradually decreases with the increase in DPA concentration. When [DPA]:[PtTPBP] = 6000:1, the fast component shows a phosphorescence lifetime of PtTPBP being 3.4 μs, much shorter than the initial lifetime of 39.1 μs (Supplementary Fig. 2a). This demonstrates that, although the DPA triplet level is a bit higher than that of PtTPBP, it is still possible to enable the TTET process through thermal-assisted mechanism[35,41]. In the BDP/PtTPBP system, the emission decay of the fast component is more significant (Supplementary Fig. 2b), which relates to the larger $K_{SV}$ and $k_{TTET}$. Therefore, if we integrate the synergistic luminescence of BDP and DPA simultaneously in the upconversion process, a higher concentration of DPA is required to regulate the competitive relationship between them.

Encouraged by those results, we studied the dual-annihilator model combining DPA and BDP with PtTPBP. As depicted in Fig. 2e and f, an obvious GSB of PtTPBP at 430 nm and a weaker positive signal at 460 nm were observed in the TA spectra. After 3.6 μs, the SE of BDP appeared at 525 nm. Those results are consistent with the mono-annihilator systems, indicating the dual-path energy transfer in the dual-annihilator system. Therefore, we simulated the efficiency of TTET of the dual-annihilator system based on Eq. 1. Figure 2g showcases the calculated $\Phi_{TTET}$ at different concentrations of DPA (0–5.0 × 10⁻² mol L⁻¹) and BDP (0 − 2.5 × 10⁻⁴ mol L⁻¹). For experimental proof, we gradually added BDP into the DPA/PtTPBP system and gained the $\Phi_{TTET}$ values in saturated ([DPA]:[PtTPBP] = 5000:1) and unsaturated ([DPA]:[PtTPBP] = 500:1) states. As shown in Table 1, the experimental results have good agreement with the calculated values, the relative errors are all less than 4.5% (($\Phi_{TTET}$−calculated $\Phi_{TTET}$)/calculated $\Phi_{TTET}$)| × 100%). In addition, we also fitted the decay of TA spectra and found that the $\Phi_{TTET}$ of the dual-annihilator model has good agreement with the proposed equation (error -1.4%, Supplementary Fig. 8). This demonstrates the accurate simulation of our dual-path energy flow in the dual-annihilator model. In addition, it is found that increasing the concentration of BDP can significantly promote the energy utilization of the sensitizer, thus improving the total TTET efficiency. Furthermore, the individual $\Phi_{TTET}$ of DPA or BDP was calculated based on their concentration through a weighted method

$$\left( \Phi_{ET-DPA} = \Phi_{TTET} \left( \frac{k_{ET1} C_{(DPA)}}{(k_{ET2} C_{(BDP)} + (k_{ET1} C_{(DPA)})} \right) \right)$$

(Fig. 2h and i). We assert that the energy flow equation of the dual-annihilator model possesses universal applicability, offering guidance for the construction and design of upconversion platforms with adjustable UCPL colors.

## Color customization of TTA-UCCPL in toluene solutions and CLCs microenvironment

The dual-annihilator model shows a very clear distinction of emission color between UCPL and DSPL with high tunability due to different abilities of DPA and BDP from sensitizer (Fig. 3a and Supplementary

Fig. 9a). The UCPL undergoes a progressive color shift from blue to yellow-green at varying ratios, while the substantial presence of DPA ensures blue fluorescence upon 365 nm excitation (as illustrated in the insets of Fig. 3a and Supplementary Fig. 8a). To capitalize on this emission color variation, we derived fitting equations correlating the molar quantity of BDP with the CIE (x, y) coordinates under both saturated (Fig. 3b and Supplementary Equations 11, 12) and unsaturated (Supplementary Fig. 9b and Supplementary Equations 13, 14) conditions. Leveraging these relationships, we made an effort to integrate the multicolor variability into CLCs to facilitate the design of tunable UCPL and UCCPL. As a starting point, we presented the building of the TTA-UCCPL platform with high $g_{lum}$ (DPA/PtTPBP and BDP/PtTPBP, Supplementary Note 3) in CLCs. Furthermore, we co-assembled the dual-annihilator model with CLCs to solve the limitation of UCPL color and multi-dimensional information security. It is worth noting that, X-ray diffraction results show that CLCs doped with the dual-annihilator model exhibit diffraction patterns similar to those of the original LCs (SLC1717) and CLCs (Supplementary Fig. 10). This indicates that the doping of DPA, BDP, and PtTPBP has no harmful effect on the behavior of liquid crystal molecules in CLCs. Since only the microenvironment of the dual-annihilator model was changed, we employed a correction factor, which is based on the dielectric constants of CLCs and toluene, to Supplementary Equation 12 then obtaining Supplementary Equation 15 (Supplementary Note 2). Applying the condition of 4/600-DPA (i.e., 4 wt% DPA/SLC1717 and [DPA]: [PtTPBP] = 600:1), we simulated six groups of chiral samples with CIE (x, y) chromaticity coordinates of (0.18, 0.17), (0.22, 0.39), (0.23, 0.43), (0.24, 0.51), (0.25, 0.54) and (0.28, 0.63), respectively. According to Supplementary Equation 15, the molar ratios of DPA/BDP are deduced to be 30000:2, 30000:8, 30,000:10, 30,000:12, 30,000:14, and 30,000:20, respectively (Fig. 3d). Interestingly, the average error between the simulation results and the experimental values about x in CIE (x,y) chromaticity coordinates was less than 5% among the six sample groups (Fig. 3e). Therefore, the dielectric constant corrected equation shows extremely high accuracy. Upon excitation of a 639 nm laser, the samples show different colors of UCCPL, while under 365 nm excitation, only blue DSCPL was observed (Fig. 3c). This enables a dramatic differentiation of emission color between UCCPL and DSCPL in a chiral microenvironment. In the following, the optical activities of this chiral dual-annihilator model were investigated.

The chiral microenvironment results from the precise regulation of the photonic bandgap (Supplementary Fig. 11). The polarizing optical microscopy images show the planar chiral texture of each R and S samples in a clear polarization pattern (Supplementary Fig. 12). In addition, a uniform distribution of the annihilators was found under fluorescence microscopy in different-channel reflection patterns (Supplementary Figs. 13 and 14). At this point, we obtained a pair of mirror-

## Table 1 | Comparison of calculation and experimental error on Φ_TTET

| DPA/BDP (DPA/PtTPBP= 5000:1) | $\Phi_{TTET}$[a] (%) | Calculated $\Phi_{TTET}$[b] (%) | |Error|[c] (%) | DPA/BDP (DPA/PtTPBP= 500:1) | $\Phi_{TTET}$ (%) | Calculated $\Phi_{TTET}$ (%) | |Error|[c] (%) |
|---|---|---|---|---|---|---|---|
| 50 | 95.67 | 95.61 | 0.06 | 5 | 93.02 | 95.01 | 2.10 |
| 100 | 92.72 | 92.87 | 0.16 | 25 | 76.77 | 80.31 | 4.40 |
| 200 | 88.96 | 90.97 | 2.21 | 50 | 68.93 | 68.84 | 0.13 |
| 400 | 85.13 | 87.19 | 2.36 | 100 | 57.73 | 56.02 | 3.05 |
| 600 | 83.18 | 85.59 | 2.81 | 200 | 46.64 | 44.64 | 4.48 |
| 800 | 82.00 | 82.37 | 0.45 | 400 | 36.00 | 36.41 | 1.13 |
| 2000 | 79.40 | 79.87 | 0.59 | 600 | 32.50 | 33.09 | 1.78 |
| -- | -- | -- | -- | 1000 | 28.93 | 30.18 | 4.14 |

[a]Experimentally, the efficiency of TTET is obtained by the equation $\Phi_{TTET} = 1 - \tau/\tau_0$, where $\tau_0$ and $\tau$ are the lifetime of the sensitizer with and without the annihilator, respectively. [b]Calculated $\Phi_{TTET}$ based on Eq. 1. [c]|Error | = |(($\Phi_{TTET}$ − calculated $\Phi_{TTET}$)/calculated $\Phi_{TTET}$)| × 100%.
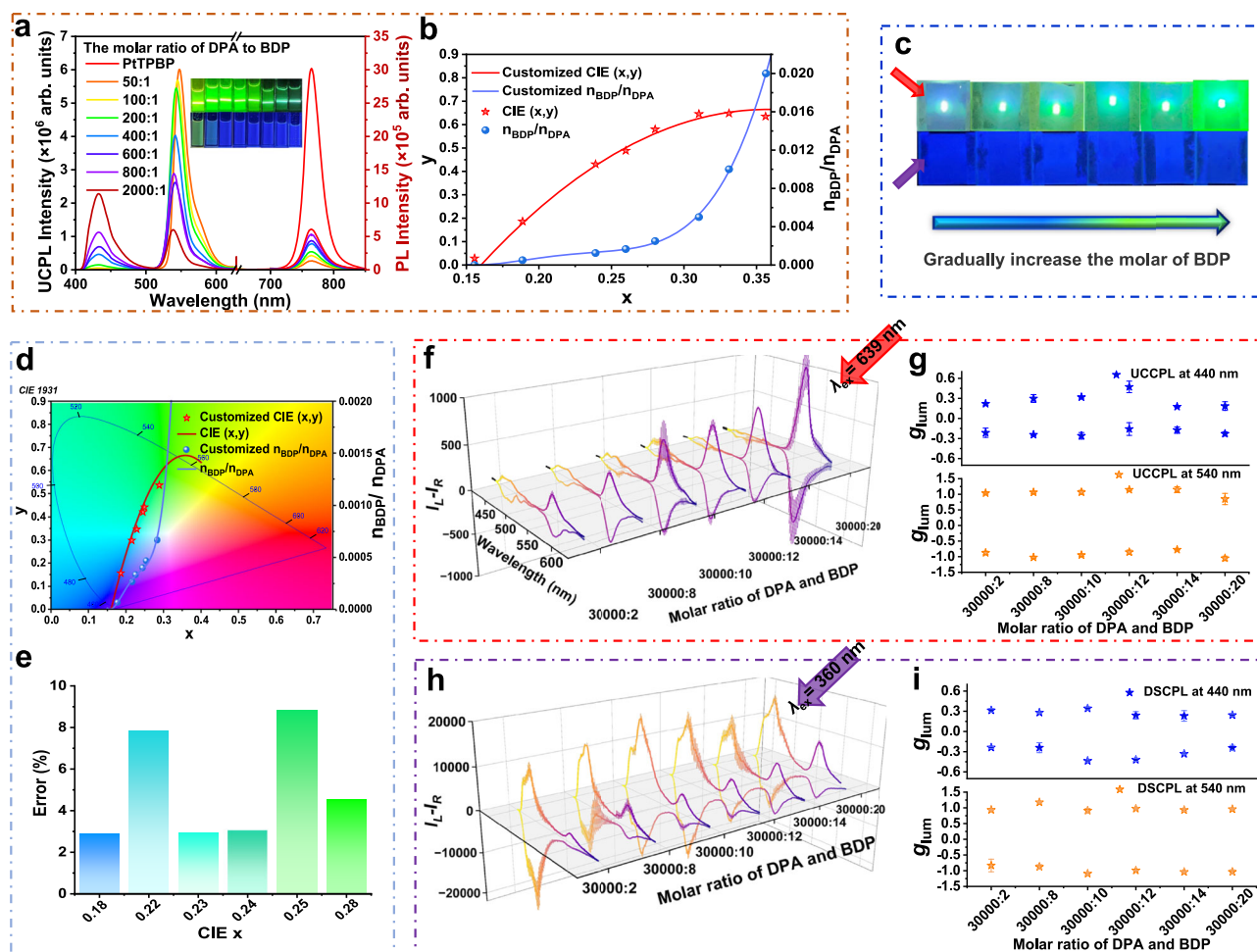
**Fig. 3 | Color design of UCPL in deaerated toluene and chiral liquid crystals (CLCs). a** UCPL spectra of dual-annihilator model as a function of different molar ratios of DPA to BDP under excitation of 639 nm laser with a power density of 2.3 W cm$^{-2}$. [PtTPBP] = 1.0 × 10$^{-5}$ mol L$^{-1}$, [DPA] = 5.0 × 10$^{-2}$ mol L$^{-1}$. Insets show the luminescence of the sample under different light sources. The uppers are illuminated by 639 nm laser while the lowers are illuminated by 365 nm light. **b** CIE (x, y) chromaticity coordinate of dual-annihilator model with varying concentrations of BDP in deaerated toluene. The relationship of x value (x in CIE (x, y) chromaticity coordinate) and [BDP]/[DPA] (blue line) as well as x and y values (y in CIE (x, y) chromaticity coordinate) (red line) was fitted. **c** Photographs of chiral dual-annihilator model with different BDP contents (the molar ratios of DPA/BDP from left to right are 30,000:2, 30,000:8, 30,000:10, 30,000:12, 30,000:14, and 30,000:20, respectively) illuminated by different light sources, uppers: 639 nm, lowers: 365 nm. **d** CIE (x, y) chromaticity coordinate of chiral dual-annihilator model with varying concentrations of BDP in CLCs. The relationship of x value and [BDP]/[DPA] (blue line) as well as x and y values (red line) was fitted. **e** The relative error diagram of the experimental data and the calculated results of the x values point in the CIE (x, y) chromaticity coordinates. **f** UCPL spectra of the above six samples ($\lambda_{ex}$ = 639 nm). **g** $g_{lum}$ values corresponding to the UCCPL at 440 and 550 nm, respectively. **h** DSCPL spectra of the above six samples ($\lambda_{ex}$ = 360 nm). **i** $g_{lum}$ values correspond to the DSCPL at 440 and 550 nm, respectively. The above spectrum of DSCPL and UCCPL was tested three times. All error bars show mean ± standard deviation. $n$ = 3 independent experiments.

image UCCPL and DSCPL signals at 440 nm and 550 nm (Fig. 3f and h), with |$g_{lum}$| around 0.3 and 1.0, respectively (Fig. 3g and i). This dual-annihilator model, with its large $g_{lum}$ values, allows for manipulation of CPL color through changing the excitation light source. Therefore, the anti-counterfeiting encryption applications based on this model, introducing an additional layer of security through polarization and varying photoluminescence colors, are expected.

## Application of the chiral dual-annihilator model in anti-counterfeiting encryption

Because the application based on TTA-UCCPL is still relatively scarce at present[26], therefore, the unique photophysical properties of the dual-annihilator model, constructed within chiral media, are utilized to explore advanced information encryption and anti-counterfeiting. As illustrated in Fig. 4a, the changeable excitation source, polarization, and varied emission colors are combined within the international Morse code to encode meaningful information. The CLCs are injected into the

micromatrix template according to the encoded data (fabrication details provided in the Methods section). Following the encryption protocol, all micromatrices emit blue fluorescence upon excitation of 365 nm light. While upon exposure to the 639 nm (reading beam), the micromatrices display different colors of UCPL. Decoding through the Morse code book reveals a deceptive message "LOVGZGY!". This encryption strategy uses UCPL to present misleading information, while the actual message is concealed within the polarization characteristic. Only using the 639 nm reading beam and a circular polarizer filter (CPF) can read out the true message: "I LOVE NANO!" (Fig. 4a). Compared to traditional TTA-UC systems for anti-counterfeiting and encryption, the chiral dual-annihilator system provides multiple layers of encryption, e.g., excitation light, polarization, and Morse code, greatly enhancing the security of information. In addition, we have incorporated added security features into encrypted images. Unlike previous TTA-UCCPL technologies[42], which struggled with distinguishing upconverting and downshifting luminescence colors, the dual-annihilator system enables
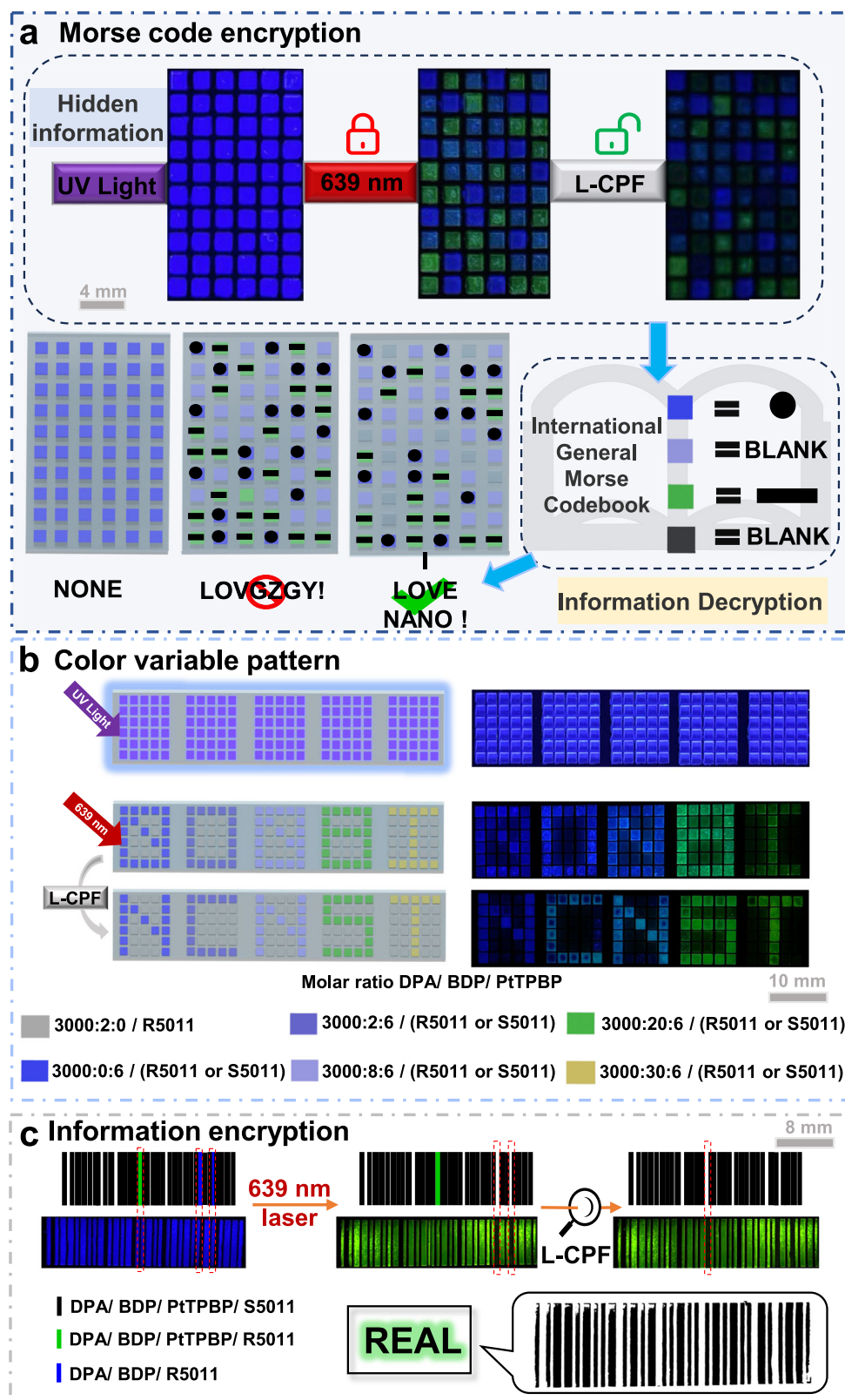
**Fig. 4 | Anti-counterfeiting and information encryption based on the micromatrices of the chiral dual-annihilator model. a** Information encryption based on the chiral dual-annihilator model combined with Morse code. **b** Similarly, the chiral dual-annihilator model with different UCCPL colors is injected into the micromatrices to realize the "NCNST" information of different colors that can be read under the 639 nm reading beam and CPF. **c** Encrypted barcode based on the chiral dual-annihilator model can quickly read the hidden "REAL" information by setting the green luminescence threshold of the UCCPL under CPF and converting it into a black and white bar graph.
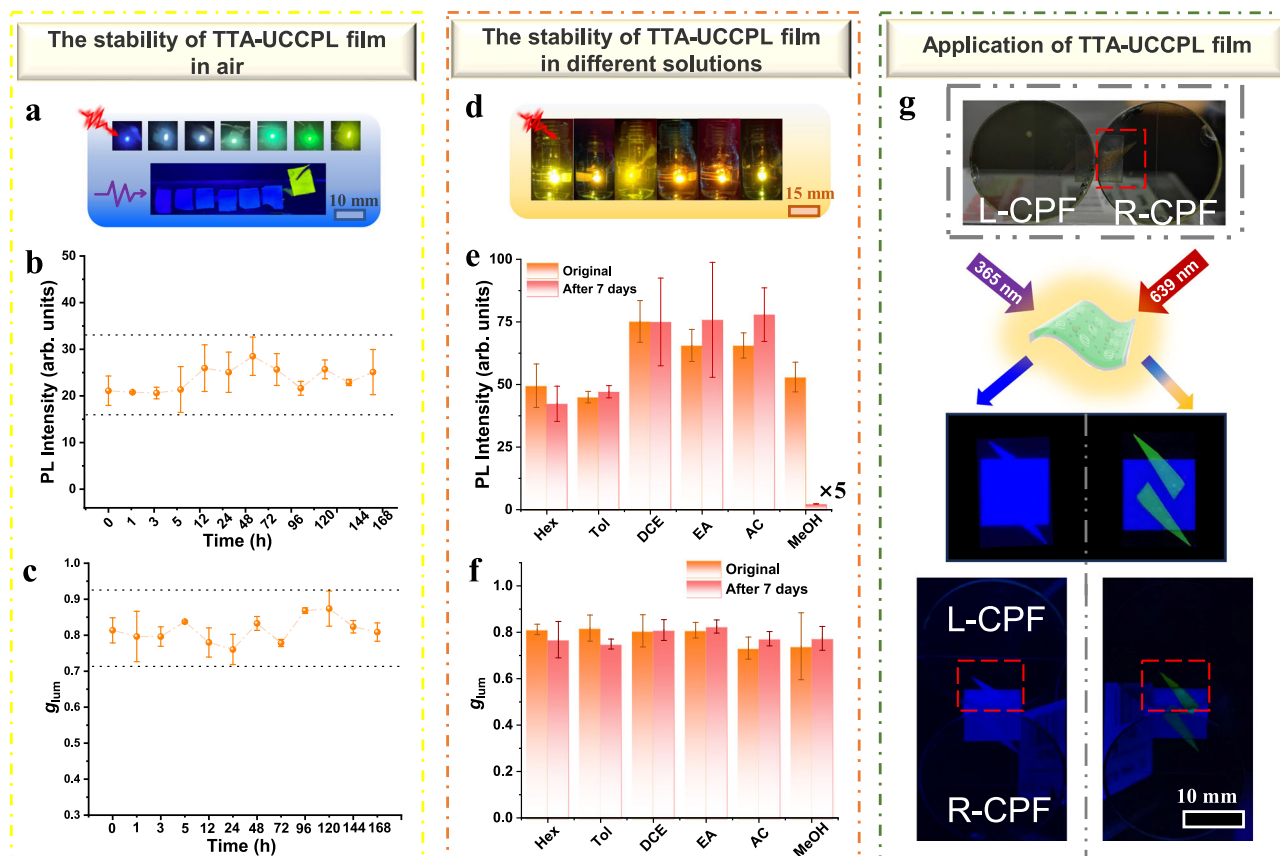
**Fig. 5 | Flexible TTA-UCCPL films were prepared to demonstrate its long-term chirality and luminescence stability in air and different common solvents and its application was explored. a** Photographs of chiral flexible TTA-UCCPL films under different excitation light sources. 639 nm photoexcitation (top) and 365 nm photoexcitation (bottom). The films from left to right are DPA/PtTPBP (4/600-DPA), 4/600-DPA/BDP ([DPA]/[BDP] = 30,000:4), 4/600-DPA/BDP ([DPA]/[BDP] = 30,000:8), 4/600-DPA/BDP ([DPA]/[BDP] = 30,000:12), 4/600-DPA/BDP ([DPA]/[BDP] = 30000:16), 4/600-DPA/BDP ([DPA]/[BDP] = 30,000:20), BDP/PtTPBP (1/100-BDP). Excited by 639 nm laser, **b, c** UCPL spectra (**b**) and $g_{lum}$ spectra (**c**) stability within 7 days were tested. **d** Photographs of chiral flexible TTA-UCCPL films in different solvents with 639 nm laser. Take the TTA-UC system of BDP/PtTPBP as an example. From left to right, the solvents are n-hexane (Hex), toluene (Tol), dichloroethane (DCE), ethyl acetate (EA), acetone (AC), and methanol (MeOH). Excited by 639 nm laser, **e, f** UCPL spectra (**e**) and $g_{lum}$ spectra (**f**) stability within 7 days were tested. **g** Chiral flexible TTA-UCCPL films with the long-term stability of different UCCPL colors were cut into the desired pattern and combined to form the logo of the NCNST (blue substrate and yellow wings). All error bars show mean ± standard deviation. $n$ = 3 independent experiments.

precise control over emission colors. The DSCPL exhibits a pure blue color, while UCPL displays a range of distinct colors (Fig. 4b), creating a complex and difficult-to-replicate anti-counterfeiting mechanism. The encryption and anti-counterfeiting pattern "NCNST" can only be correctly viewed when the reading beam and CPF are used together, with each letter's unique color enabling dual-level security for both encryption and anti-counterfeiting purposes[43].

The cryptographic potential of the dual-annihilator model extends well beyond its current use cases. Quick-response (QR) codes, which are two-dimensional barcodes rich in data, can be easily decoded but are easy to conterfeiting[44]. To address this issue, it is critical to imbue QR codes with anti-counterfeiting features. As shown in Fig. 4c, the correct QR code information can be retrieved through the interaction of the reading beam and CPF. By setting an emission brightness threshold (brightness value: 255) in Python, only the green emission is converted to a black barcode, facilitating the rapid decoding of information and enhancing QR code security through emission color differences. This dual-function approach not only strengthens the QR code's resistance to counterfeiting but also embodies the sophisticated integration of DSPL, UCPL, and UCCPL technologies. The resulting system represents a significant advancement in secure information encryption and anti-counterfeiting, providing a powerful solution with wide-reaching potential.

## Stability and machinability of chiral flexible TTA-UCCPL films

The challenging conditions for achieving TTA-UC, such as the need for a liquid medium to facilitate exciton migration and the requirement to isolate oxygen[45,46], have significantly hindered their practical applications[20,47,48]. To address these limitations, we have developed chiral flexible TTA-UCCPL films that exhibit both long-term air stability and solvent resistance (Supplementary Fig. 15)[49–51]. As illustrated in Fig. 5a, these films exhibit distinct differences between UCPL and DSPL across various dual-annihilator models, indicating their strong potential for tunable CPL color applications. To further assess the stability and practical viability of these flexible films, we selected the 1/100-BDP system (1 wt% BDP/SLC1717 and [BDP]/[PtTPBP] = 100:1) as a case study. After 7 days of exposure to air, both UCPL and chirality remained stable, with the |$g_{lum}$| value fluctuating reasonably between 0.75 and 0.85 (Fig. 5b, c, and Supplementary Fig. 16). In order to meet the requirements of practical applications, the film performances were also tested in various organic solvents. As shown in Fig. 5d, bright UCPL remains even when the film is immersed in different solvents. In methanol, the swelling of the polymer film compromised its oxygen-shielding capability. Given the inherent oxygen sensitivity of the TTA-UC system, this structural modification allowed gradual oxygen permeation into the swollen matrix. Consequently, the UCPL intensity decreased by 20% within the first 3 hours of exposure. This

degradation process continued progressively, ultimately leaving only residual UCPL signals after 7 days of sustained oxygen infiltration through the compromised polymer structure. In contrast, the other five solvents maintained excellent stability for both UCPL and $|g_{lum}|$ over extended periods (Fig. 5e, f and Supplementary Figs. 17–22). With their long-term air stability and solvent resistance, these films effectively address key challenges related to environmental sensitivity and operational stability. These remarkable properties lead us to further explore their potential applications. We fabricated films with photonic bandgap positions at 440 and 550 nm, and precisely tailored them to create the logo of The National Center for Nanoscience and Technology, featuring a blue substrate and yellow wings (Fig. 5g). Under visible light, the photonic bandgap effect causes a clear contrast in brightness between the logo's elements when viewed through left and right CPF. When illuminated with 365 nm light, the logo is hidden, but it could be effectively revealed under 639 nm light with CPF. These results demonstrate the practical feasibility of these films and the intriguing heterochromatic phenomena they exhibit, paving the way for broader and deeper applications in the future.

## Discussion

In summary, the proposed dual-annihilator model expands the regulation of luminescence gamut in the TTA-UC system with the help of the dual-channel energy transfer design. In this work, we propose coupled equations for estimating the energy flow of the model and then apply them to TTA-UCCPL color design. Additionally, the combination of the upconversion emission tunability brought by the dual-path structure and the CLCs makes it possible for potential applications in optical information security. It is demonstrated that high-level and multi-dimension anti-counterfeiting patterns, graphical encoding, and flexible chiral film can be fabricated. Through this model, our research shows how to use an asymmetric energy transfer process to achieve multi-dimensional optical regulation, marking the profound exploration of TTA-UC information encryption anti-counterfeiting applications.

## Methods

### Materials

The emitter (9,10-Diphenylanthracene, DPA) was purchased from Shanghai Aladdin Biochemical Technology Co., LTD. Another emitter (4-(prop-2-yn-1-yloxy)-boradiazaindacene, BDP) was synthesized according to the method in reference 52[52]. Pt(II) mesotetraphenyl tetrabenzoporphine (>95%) was purchased from Frontier Scientific, Inc. Commercial room-temperature nematic liquid crystal, SLC1717, was bought from the Chengzhi Yonghua Display Material Co., Ltd. Polymer precursor 2-methyl-1,4-phenylene bis(4-((6-(acryloyloxy)-hexyl)oxy)benzoate) (C6M, 97%), cross-linking agent trimethylolpropane triacrylate (TMPTA, 95%), and photoinitiator 2,2-dimethoxy-2-phenylacetophenone (I-651, 99%) were purchased from Merck. The chiral dopant S (or R)5011 (>98%) was provided by Jiangsu Hecheng Display Technology Co., Ltd. Cleaned glass slides were used to prepare liquid crystalline cells. The conventional reagents and solvents used were purchased from the public platform and the National Pharmaceutical Reagent Company and were not purified and used directly.

### Characterizations

The $^1$H NMR and $^{13}$C NMR spectra were recorded on a Bruker Avance III 400 HD spectrometer. High-resolution mass spectra (HRMS) were obtained on a Finnigan MAT TSQ 5800 Mass Spectrometer System operated in a MALDI-TOF mode. UV–Vis spectra were recorded in quartz cuvettes on a U-3900 spectrophotometer. Upconverted emission decays were recorded on a HORIBA Scientific Nanolog FL3-iHR320 spectrofluorometer using multichannel scaling. Fluorescence spectra were obtained using EDINBURGH FS5 Spectrofluorometer. Fluorescence lifetime measurements were recorded on the Edinburg

FS5 fluorescence spectrometer using time-correlated single photon counting (TCSPC). Transient absorption spectra were measured on Vitara T-Legend EliteTOPAS-Helios-EOS-Omni spectrometer supported by Technical Institute of Physics and Chemistry, CAS. Circular Dichroism (CD) spectra were recorded in quartz curettes on a JASCO J-1500 spectrophotometer. CPL spectra for single-component studies measurements were performed with a JASCO CPL-200 spectrometer. To keep the detector at the best state and obtain the precise signals, the DC values were monitored to about 0.5 Voltage. Upconverting and downshifting photoluminescence and CPL measurements were performed on a monochromator equipped with a charge-coupled device detector (Andor Technology, iVac 316). 639 nm continuous wave laser was chosen for excitation. The detection of CPL is set according to the description in Supplementary Fig. 27. Typically, the emissive light of samples passed through an achromatic broadband quarter-waveplate, which was used to separate the left (L, having intensity $I_L$) and right (R, having intensity $I_R$) circularly polarized components. The DS-/ UC-CPL signal was calculated as DS-/ UC-CPL $= I_L - I_R$. Polarizing optical microscopy (POM) was recorded on the Olympus X83 using a high-pressure mercury lamp as an excitation source for fluorescent images. The schematic figures in this manuscript were drawn by the first author in Microsoft PowerPoint and Blender. Python Software Uses Spyder 5.4.3.

### Synthesis of compound BDP

To a 250 mL round-bottomed flask containing 20 mL argon-degassed dichloromethane were added 3-ethyl-2,4-dimethyl pyrrole (595 mg, 4.82 mmol) and propargyl benzaldehyde (350 mg, 2.19 mmol). One drop of TFA was added, and the solution was stirred under a nitrogen atmosphere at room temperature for 24 h. 2,3-Dichloro-5,6-dicyano-1,4-benzoquinone (504 mg, 2.19 mmol) diluted with dichloromethane (50 mL) was added to the reaction solution, stirred for 30 min, followed by NEt$_3$ (2.5 mL) and BF$_3 \cdot$ OEt$_3$ (2.5 mL), and continued to react at room temperature for 30 min. At the end of the reaction, the reaction liquid was evaporated by rotation, extracted three times using dichloromethane and water (3 × 100 mL), collected the organic phase, dried with anhydrous MgSO$_4$, and evaporated by rotation. Subsequently, the raw product was separated by column chromatography (dichloromethane/petroleum ether = 2:1) to achieve 275 mg of the target compound BDP. Yield 28%. $^1$H NMR (400 MHz, CDCl$_3$) $\delta$ 7.22 (d, $J = 8.6$ Hz, 2H), 7.10 (d, $J = 8.6$ Hz, 2H), 4.79 (d, $J = 2.3$ Hz, 2H), 2.59 (s, 1H), 2.55 (s, 6H), 2.32 (q, $J = 7.5$ Hz, 4H), 1.35 (s, 6H), 1.00 (t, $J = 7.5$ Hz, 6H). $^{13}$C NMR (101 MHz, CDCl$_3$) $\delta$ 157.93, 153.60, 139.91, 138.41, 132.71, 131.09, 129.49, 129.36, 128.84, 115.52, 75.86, 56.03, 17.08, 14.66, 12.51, 11.84. Maldi-TOF: calculated for C$_{26}$H$_{29}$BF$_2$N$_2$O: [M] = 434.2341; found: [M] = 434.2351.

### Preparing samples of the TTA-UC system in solution

Deaerated toluene was prepared by freezing and thawing toluene with liquid nitrogen and replacing air with nitrogen. Then prepare TTA-UC system samples in a glove box, use the prepared deaerated toluene to dissolve the samples in a plug cuvette (1 mm × 1 cm), and seal the opening with a hot melt gun. All tests were carried out in the air.

### Preparation of chiral dual-annihilator model liquid crystal cell (LC cell)

An empty liquid crystal cell is made by attaching two quartz sheets to both sides through spacers. Prepare toluene solutions of annihilators ([DPA] = 0.1 mol L$^{-1}$, [BDP] = 4.0 × 10$^{-3}$ mol L$^{-1}$) and sensitizer ([PtTPBP] = 2.0 × 10$^{-5}$ mol L$^{-1}$). A CLCs mixture containing 10 mg commercial eutectic nematic LC (SLC1717), 0.27 ~ 0.33 mg chiral dopants (R5011 or S5011), and the corresponding toluene solution of the TTA model were uniformly mixed. The mixture was heated to 80 °C and filled in an LC cell (thickness was 20 μm) by capillary action. Then annealing was carried out at a rate of 0.5 °C per minute. All the above sample preparation and testing using LC cells are carried out in the air.

## Preparation of chiral dual-annihilator model micromatrices

Using a laser marking machine (UV-50) purchased from Changchun New Industry Optoelectronic Technology Co., Ltd., to mark grooves with encrypted information and patterns on a clean quartz substrate. According to the encryption protocol, different dual-annihilator molecules prepared above are selectively filled into the corresponding matrix to achieve information customization and encryption. Information encryption and anti-counterfeiting pattern production are equivalent to the LC cell environment, and they are also prepared and displayed in the air.

## Preparation of flexible dual-annihilator model films

A CLCs mixture containing 10 mg SLC1717, 0.10-0.25 mg chiral dopants (R5011 or S5011), 5 mg reactive mesogen (C6M), 0.78 mg crosslinking agent (TMPTA), 0.25 mg photoinitiator (I-651), and different dual-annihilator molecules prepared above was homogeneously mixed in a chloroform solution. The mixture was heated to 80 °C and filled in an LC cell (thickness was 20 μm) by capillary action. Then annealing was carried out at a rate of 0.5 °C per minute. Afterward, the sample was exposed to UV irradiation (365 nm) for 21 min to polymerize the orderly arranged C6M and TMPTA; Remove the LC cell. Finally, the film was dipped into a 10 wt% PVA aqueous solution to evenly cover the surface of the film with dense PVA and then placed at room temperature overnight to obtain a flexible dual-annihilator model film. All the above operations for preparing flexible dual-annihilator model films are carried out in the air.

## Reporting summary

Further information on research design is available in the Nature Portfolio Reporting Summary linked to this article.

## Data availability

All data supporting this study, including detailed methods and experimental details, photophysical properties studies, are available in the Manuscript, Supplementary information, and Source Data file. All data are available upon request. Source data are provided with this paper.

## References

1. Bharmoria, P. et al. Triplet–triplet annihilation based near infrared to visible molecular photon upconversion. *Chem. Soc. Rev.* **49**, 6529–6554 (2020).
2. Ha, D. et al. Exchange controlled triplet fusion in metal–organic frameworks. *Nat. Mater.* **21**, 1275–1281 (2022).
3. Han, J. et al. Amplification of circularly polarized luminescence through triplet-triplet annihilation-based photon upconversion. *J. Am. Chem. Soc.* **139**, 9783–9786 (2017).
4. Zhang, Q. et al. Crystalline hydrogen-bonded organic framework for air-tolerant triplet–triplet annihilation upconversion. *Chem. Commun.* **60**, 4475–4478 (2024).
5. Li, J. et al. NIR-Absorbing B,N-Heteroarene as photosensitizer for high-performance NIR-to-blue triplet-triplet annihilation upconversion. *Angew. Chem. Int. Ed.* **62**, e202303093 (2023).
6. Monguzzi, A. et al. Low-power-photon up-conversion in dual-dye-loaded polymer nanoparticles. *Adv. Funct. Mater.* **22**, 139–143 (2011).
7. Huang, L. et al. Triplet–triplet annihilation photon upconversion-mediated photochemical reactions. *Nat. Rev. Chem.* **8**, 238–255 (2024).
8. Carrod, A. J. et al. Recent advances in triplet–triplet annihilation upconversion and singlet fission, towards solar energy applications. *Energ. Environ. Sci.* **15**, 4982–5016 (2022).
9. Gao, C. et al. Application of triplet–triplet annihilation upconversion in organic optoelectronic devices: advances and perspectives. *Adv. Mater.* **33**, 2100704 (2021).
10. Healy, C. et al. Photon upconversion in self-assembled materials. *Coord. Chem. Rev.* **432**, 213756 (2021).
11. Monguzzi, A. et al. Upconversion-induced delayed fluorescence in multicomponent organic systems: Role of Dexter energy transfer. *Phys. Rev. B* **77**, 155122 (2008).
12. Mongin, C. et al. Direct observation of triplet energy transfer from semiconductor nanocrystals. *Science* **351**, 369–372 (2016).
13. Ye, C. et al. Annihilation versus excimer formation by the triplet pair in triplet–triplet annihilation photon upconversion. *J. Am. Chem. Soc.* **141**, 9578–9584 (2019).
14. Sanders, S. N. et al. Triplet fusion upconversion nanocapsules for volumetric 3D printing. *Nature* **604**, 474–478 (2022).
15. Zhao, T. et al. Amplifying dissymmetry factor of upconverted circularly polarized luminescence through chirality-induced spin polarization in the photon upconversion process. *J. Phys. Chem. Lett.* **11**, 311–317 (2019).
16. Stich, D. et al. Triplet–triplet exciton dynamics in single-walled carbon nanotubes. *Nat. Photon.* **8**, 139–144 (2013).
17. Fan, C. et al. Enhanced triplet–triplet energy transfer and upconversion fluorescence through host–guest complexation. *J. Am. Chem. Soc.* **138**, 15405–15412 (2016).
18. Ogawa, T. et al. Donor–acceptor–collector ternary crystalline films for efficient solid-state photon upconversion. *J. Am. Chem. Soc.* **140**, 8788–8796 (2018).
19. Bossanyi, D. G. et al. Emissive spin-0 triplet-pairs are a direct product of triplet–triplet annihilation in pentacene single crystals and anthradithiophene films. *Nat. Chem.* **13**, 163–171 (2020).
20. Cho, H. H. et al. Efficient near-infrared organic light-emitting diodes with emission from spin doublet excitons. *Nat. Photon.* **18**, 905–912 (2024).
21. Jiang, L. et al. Near infrared-II excited triplet fusion upconversion with anti-Stokes shift approaching the theoretical limit. *J. Am. Chem. Soc.* **146**, 10785–10797 (2024).
22. Li, L. et al. Thermally activated delayed fluorescence via triplet fusion. *J. Phys. Chem. Lett.* **10**, 6239–6245 (2019).
23. Yao, W. et al. Tunable emissions of upconversion fluorescence for security applications. *Adv. Opt. Mater.* **7**, 1801171 (2018).
24. Wang, J. X. et al. Triplet-triplet energy-transfer-based transparent X-ray imaging scintillators. *Matter* **6**, 217–225 (2023).
25. Li, F. et al. Size-dependent lanthanide energy transfer amplifies upconversion luminescence quantum yields. *Nat. Photon.* **18**, 440–449 (2024).
26. Han, D. et al. Sequentially amplified circularly polarized ultraviolet luminescence for enantioselective photopolymerization. *Nat. Commun.* **11**, 5659 (2020).
27. Mori, T. Significance of vibronic coupling that shapes circularly polarized luminescence of double helicenes. *Angew. Chem. Int. Ed.* **63**, e202319702 (2024).
28. Crassous, J. et al. Materials for chiral light control. *Nat. Rev. Mater.* **8**, 365–371 (2023).
29. Wu, Y. et al. Liquid crystal assembly for ultra-dissymmetric circularly polarized luminescence and beyond. *J. Am. Chem. Soc.* **145**, 12951–12966 (2023).
30. Zhang, M. et al. Amplifying inorganic chirality using liquid crystals. *Nanoscale* **14**, 592–601 (2022).
31. Yang, X. F. et al. Dual band-edge enhancing overall performance of upconverted near-infrared circularly polarized luminescence for anticounterfeiting. *ACS Nano* **17**, 2661–2668 (2023).
32. Monguzzi, A. et al. Upconversion-induced fluorescence in multicomponent systems: Steady-state excitation power threshold. *Phys. Rev. B* **78**, 195112 (2008).
33. Naimovičius, L. et al. The statistical probability factor in triplet mediated photon upconversion: a case study with perylene. *J. Mater. Chem. C* **11**, 14826–14832 (2023).

34. Bao, G. et al. Hidden triplet states at hybrid organic–inorganic interfaces. *Nat. Rev. Chem.* **10**, 28–43 (2025).

35. He, S. et al. Entropy-gated thermally activated delayed emission lifetime in phenanthrene-functionalized CsPbBr3 Perovskite nanocrystals. *J. Phys. Chem. Lett.* **12**, 8598–8604 (2021).

36. Zhang, X. et al. Liquid crystal-templated chiral nanomaterials: from chiral plasmonics to circularly polarized luminescence. *Light Sci. Appl.* **11**, 223 (2022).

37. Li, Y. et al. Light-driven sign inversion of circularly polarized luminescence enabled by dichroism modulation in cholesteric liquid crystals. *Adv. Mater.* **36**, 2312331 (2024).

38. Cheng, X. et al. Switchable phase helicity independent of the absolute configuration of the stereocenter: anomalous induction between sergeants and soldiers in chiral liquid-crystalline polymers. *J. Am. Chem. Soc.* **145**, 16474–16487 (2023).

39. Wu, Y. et al. Circularly polarized Fluorescence Resonance Energy Transfer (C-FRET) for efficient chirality transmission within an intermolecular system. *Angew. Chem. Int. Ed.* **60**, 24549–24557 (2021).

40. Zhang, M. et al. Processable circularly polarized luminescence material enables flexible stereoscopic 3D imaging. *Sci. Adv.* **9**, eadi9944 (2023).

41. He, S. et al. Entropy-powered endothermic energy transfer from CsPbBr3 nanocrystals for photon upconversion. *J. Phys. Chem. Lett.* **13**, 1713–1718 (2022).

42. Zhao, T. et al. Multi-light-responsive upconversion-and-downshifting-based circularly polarized luminescent switches in chiral metal–organic frameworks. *Adv. Mater.* **33**, 2101797 (2021).

43. Gu, L. et al. Circularly polarized organic room temperature phosphorescence from amorphous copolymers. *J. Am. Chem. Soc.* **143**, 18527–18535 (2021).

44. Wang, Q. et al. A dynamic assembly-induced emissive system for advanced information encryption with time-dependent security. *Nat. Commun.* **13**, 4185 (2022).

45. Wei, L. et al. Triplet–triplet annihilation upconversion in LAPONITE®/PVP nanocomposites: absolute quantum yields of up to 23.8% in the solid state and application to anti-counterfeiting. *Mater. Horiz.* **9**, 3048–3056 (2022).

46. Askes, S. H. C. et al. Solving the oxygen sensitivity of sensitized photon upconversion in life science applications. *Nat. Rev. Chem.* **2**, 437–452 (2018).

47. Xiao, X. et al. Controlling the triplet states and their application in external stimuli-responsive triplet–triplet-annihilation photon upconversion: from the perspective of excited state photochemistry. *Chem. Soc. Rev.* **50**, 9686–9714 (2021).

48. Zeng, L. et al. Long wavelength near-infrared and red light-driven consecutive photo-induced electron transfer for highly effective photoredox catalysis. *Nat. Commun.* **15**, 7270 (2024).

49. Shi, Y. et al. Recyclable soft photonic crystal film with overall improved circularly polarized luminescence. *Nat. Commun.* **14**, 6123 (2023).

50. Xu, M. et al. Exploring the circular polarization capacity from chiral cellulose nanocrystal films for a photo-controlled chiral Helix of supramolecular. *Polym. Angew. Chem. Int. Ed.* **61**, e202117042 (2022).

51. Xie, Y. et al. Inverse design of chiral functional films by a robotic AI-guided system. *Nat. Commun.* **14**, 6177 (2023).

52. Kolemen, S. et al. Optimization of distyryl-Bodipy chromophores for efficient panchromatic sensitization in dye sensitized solar cells. *Chem. Sci.* **2**, 949–954 (2011).

## Author contributions

P.D. and T.Z. conceived the idea and supervised the project. H.J., T.Z. and P.D. designed the experiments. H.J. performed the chiroptical study. H.J. and Z.L. designed, synthesized and characterized the materials. H.J. carried out the theoretical calculations. H.J., X.Y., X.J., T.Z. and P.D. wrote and revised the manuscript. All authors analysed and discussed the results and have given approval for the final version of the manuscript.

## Competing interests

The authors declare no competing interests.

## Additional information

**Supplementary information** The online version contains supplementary material available at https://doi.org/10.1038/s41467-025-60290-7.

**Correspondence** and requests for materials should be addressed to Tonghan Zhao or Pengfei Duan.

**Peer review information** *Nature Communications* thanks Gang Han, Wei-Hong Zhu, Taotao Zhuang and the other, anonymous, reviewer(s) for their contribution to the peer review of this work. A peer review file is available.

**Reprints and permissions information** is available at http://www.nature.com/reprints

**Publisher's note** Springer Nature remains neutral with regard to jurisdictional claims in published maps and institutional affiliations.